5-15-2020

Mechanical Analysis and Modeling of Porous Thermal Barrier Coatings

Shiyu Cui
Nanchang Hangkong University

Wenping Liang
Nanjing University of Aeronautics and Astronautics

Luis Saucedo Mora
Institute Eduardo Torroja of Construction Sciences

Qiang Miao
Nanjing University of Aeronautics and Astronautics

Joseph P. Domblesky
Marquette University, joseph.domblesky@marquette.edu

See next page for additional authors

Recommended Citation

Cui, Shiyu; Liang, Wenping; Mora, Luis Saucedo; Miao, Qiang; Domblesky, Joseph P.; Lin, Hao; and Yu, Lijia, "Mechanical Analysis and Modeling of Porous Thermal Barrier Coatings" (2020). *Mechanical Engineering Faculty Research and Publications*. 252.
https://epublications.marquette.edu/mechengin_fac/252

Authors

Shiyu Cui, Wenping Liang, Luis Saucedo Mora, Qiang Miao, Joseph P. Domblesky, Hao Lin, and Lijia Yu

Applied Surface Science, Vol. 512 (May 15, 2020): 145706. DOI. This article is © Elsevier and permission has been granted for this version to appear in e-Publications@Marquette. Elsevier does not grant permission for this article to be further copied/distributed or hosted elsewhere without the express permission from Elsevier.

Mechanical Analysis and Modeling of Porous Thermal Barrier Coatings

Shiyu Cui
School of Materials Science and Engineering, Nanchang Hangkong University, Nanchang 330063, China
Institute Eduardo Torroja of Construction Sciences, C\ Serrano Galvache, 4, Madrid 28030, Spain
Wenping Liang
College of Material Science and Technology, Nanjing University of Aeronautics and Astronautics, 29 Yudao Street, Nanjing 210000, China
Luis Saucedo Mora
Institute Eduardo Torroja of Construction Sciences, C\ Serrano Galvache, 4, Madrid 28030, Spain
University of Oxford, Parks Road, OX1 3PH, Oxford, UK
Qiang Miao
College of Material Science and Technology, Nanjing University of Aeronautics and Astronautics, 29 Yudao Street, Nanjing 210000, China
Joseph P. Domblesky
Department of Mechanical Engineering, Marquette University, 1515 West Wisconsin Avenue, Milwaukee, WI

Hao Lin
College of Material Science and Technology, Nanjing University of Aeronautics and Astronautics, 29 Yudao Street, Nanjing 210000, China
Lijia Yu
College of Material Science and Technology, Nanjing University of Aeronautics and Astronautics, 29 Yudao Street, Nanjing 210000, China

Abstract

Thermal barrier coatings (TBCs) are applied to the surface of components that are used in gas turbines and aircraft engines in order to increase the heat load. In this study, the cross-sectional microstructures of TBCs were investigated via scanning electron microscopy. After calculating the porosity and the pore size distribution, a two-dimensional finite element model with four different porosities (0, 1, 3, and 5%) were established. A stochastic method was used to generate a randomly distributed porous structure. Based on the results of FE analysis and nanoindentation tests, It was found that, at a high porosity (>3%), radial cracks are affected by the interaction between neighboring pores and occur at the top/bond coating interface. After the cooling stage, radial cracks continue their propagating trends. However, axial cracks are commonly generated from the ZrO_2–8 wt.%Y_2O_3 surface as the tensile stress caused by a single micro-pore can be as much as three times higher than that of its surrounding area (porosity < 3%) at 1473 K. The addition of a 20 µm sealing layer can effectively eliminate the stress effects of the micro-pores on the YSZ coating surface.

Graphical abstract

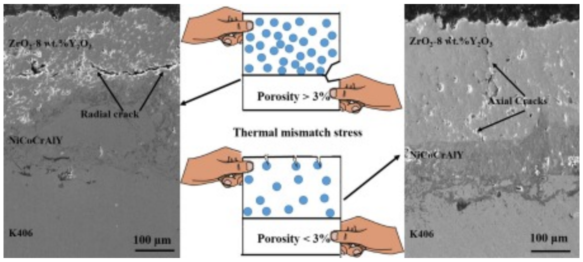

Keywords

Porosity, Thermal barrier coatings, Cracks, and compressive stress

1. Introduction

Thermal barrier coatings (TBCs) are advanced materials systems and frequently applied to the surface of engine components in order to prolong the service life and increase operating temperature [1], [2]. TBCs consist of three different regions which include: top coating (TC), bond coating (BC), and metallic substrate. Typically, TC and BC are deposited on the surface of a metallic component using thermal spraying and act to protect the substrate from large and prolonged heat loads. The barrier system is necessary due to the fact that the top coating is a ceramic with low conductivity and has a different CTE than the substrate [3]. Currently, one of the more common TBCs in use is based on the MCrAlY (M = Ni, Co, and/or Fe) system and is used as a bond coating (BC) in the TBC materials. The existing body of research work on TBCs were found to be much more stable under high-temperature conditions and provided a significant increase in service life [4].

When the operational environment is constant, the TBCs' microstructure becomes the primary factor affecting the service life. In particular, the micro-pores and cracks are the basic characteristics for the TBCs fabricated by plasma spraying [5]. The propagation of the crack is induced by the development of the thermal stress which is decided by the following factors. First, the thermal mismatch between TC, BC, and substrate can produce stress concentration easily. In addition, the sintering process of porous TC could increase the thermal conductivity coefficient which would decrease the insulation performance [6]. And finally, the non-linear behaviors of TBCs materials have a strong influence on crack growth rates [7], [8]. The non-linear coupled effects of creep, temperature gradient, and coating morphology need to be further explored for practical applications that determine the service life of high-temperature components.

Several experimental studies have been performed to investigate stress levels and distribution that develop in TBCs during service. Sujanto et al. [9] used X-ray diffraction to assess residual stresses in ZrO_2 coatings and found that the normal stress state is compressive. Zhu et al. [10] studied the compressive stress existing in the TC using Moiré interferometry and nanoindentation techniques. However, it must be considered that the above-mentioned characterizations of stress state were limited to a depth of 5 μm below the surface, and the top coating thickness is typically in excess of 200 μm in most TBCs. Owing to the difficulties associated with making accurate experimental measurements, researchers are increasingly using numerical models to analyze the stress distribution in TBCs and have found the FE method to be one of the more efficient methods for characterizing and predicting the structural behavior of whole TBCs. Wang et al. [11] reported that in the case of a surface crack, the stress at the crack tip is higher than that inside the top coating. Although global stress fields have been widely studied, the relationship between crack initiation mechanisms and the network structure of micro-pores is still not completely understood.

In the present study, a thermo-mechanical analysis of porous TBCs was carried out using a two-dimensional (2D) FE model to analyze the effects of spatial distribution and the interactions between neighboring micro-pores. In order to study the influence of micro-defects on residual stress, the actual computational model is established which is based on the cross-section image of the TBCs. The stress distribution and the mechanisms of crack generation in the TBC were analyzed at four different porosity levels (0, 1, 3, and 5%) and the model was developed using a random stochastic method. The accuracy of the FE model was verified using closed-form theoretical analyses and results obtained from nanoindentation tests. Based on the simulation results, the use of a sealed layer is proposed to eliminate the stress concentration on the TBC surface where the thickness of the sealed layer is based on the radius of micro-pores.

2. Experimental procedure

The K406 substrate is a precipitation hardening nickel-based superalloy, which is commonly used in turbine rotor blades, turning vanes, and integral impellers. The chemical composition of K406 is given in Table 1. The dimensions of the K406 samples used as substrates were Φ 20 mm × 3 mm. In this study, a ZrO_2–8 wt.%Y_2O_3 ceramic top coating and a NiCoCrAlY bond coating were deposited on a K406 superalloy substrate using a DH1080 thermal spray system. The detailed summary of the experimental parameters is presented in Table 2.

Table 1. Nominal chemical composition of the K406 substrate material used in the study.

Element	**C**	**Cr**	**Ni**	**Mo**	**Al**	**Ti**	**Fe**	**B**	**Si**	**Mn**
wt/%	0.03~0.08	18.0~19.0	The rest	4.5~6.0	3.25~4.0	2.0~3.0	≤1.00	0.05~0.10	≤0.30	≤0.10

Table 2. Summary of the plasma spray process parameter used to generate the TBCs.

Powder	**Current (A)**	**Voltage (V)**	**Argon flow rate (L/min)**	**Hydrogen flow rate (L/min)**	**Mass flow rate (g/min)**	**Spray distance (cm)**
NiCoCrAlY	450	75	55	17	35	12
ZrO_2-8 wt. %Y_2O_3	550	70	36	17	30	12

The cross-sectional morphologies of the coatings were observed by scanning electron microscopy (JSM-6360LV, JEOL, Japan). To detect the thermal stress of the TBC coating, nanoindentation tests were carried out on the TC's surface using a commercial testing machine (DHT-115, Shimadzu, Japan) with a triangular 115° pyramidal indenter. The maximum indentation force, rate of loading force, and holding time were set to 200 mN, 70 mN/min, and 10 s, respectively. To obtain a stress-free state, the TBCs sample was immersed in hydrochloric acid to dissolve the metallic substrate so that no additional stresses would be present in the top coating [10]. The residual stress in the other three samples was relieved by natural aging (293 K, 2 weeks). These three samples were heated in a furnace to 1473 K to simulate the conditions encountered during the actual service. After progressive heating for 30 min, the samples were cooled to room temperature. Finally, dozens of nanoindentation tests were performed on all the samples.

3. Analytical model

Generally, thermal stress in TBCs develops as a result of phase transformation, quenching, and thermal mismatch. A typical ZrO_2 coating will transform from tetragonal to monoclinic phase with 5% bulk expansion at elevated temperatures [12]. However, this type of stress can be suppressed by adding 8 wt% Y_2O_3 to stabilize the tetragonal phase. Therefore, the contribution of intrinsic growth stress to the final thermal stresses is typically less than that considered in previous studies [13]. Consequently, this stress component can be ignored. When the TBCs are rapidly cooled from the processing temperature to room temperature, the as-sprayed coating will contract quickly, resulting in quench stress. The magnitude of the quenching stress σ_q can be calculated according to Eq. (1) as shown [4]:

(1)

$$\sigma_q = \alpha_{TC}(T_m - T_s)E_{TC}$$

where α_{TC} is the coefficient of thermal expansion of the top coating, Tm is the melting point of the sprayed material, T_s is the substrate temperature during spraying, and ETC is Young's modulus of the top coating. However, the magnitude of the quenching stress tends to be relatively low (~10 MPa) because it is relieved by defects during the fabrication process and can also be reduced by natural aging [14]. As such, the effect of quenching stress considered negligible and is also ignored in the present study. The third stress component is the thermal mismatch stress which is caused by a difference in the coefficient of thermal expansion between dissimilar materials that can lead to premature failure of the TBC system. The thermal mismatch stress can be estimated by the following equations [9], [15]:

(2)

$$\sigma_{BC} = E_{BC}\frac{(\alpha_s - \alpha_{BC}) + 4\gamma_{TC}(\alpha_{TC} - \alpha_{BC})}{1 + 4(\gamma_{BC} + \gamma_{TC})}\Delta T$$

(3)

$$\sigma_{TC} = E_{TC}\frac{(\alpha_s - \alpha_{TC}) + 4\gamma_{BC}(\alpha_{BC} - \alpha_{TC})}{1 + 4(\gamma_{BC} + \gamma_{TC})}\Delta T$$

where σ_{BC} and σ_{TC} represent the thermal mismatch stress in the bond and the top coating, respectively. E_{BC} is Young's modulus of the bond coating, α_s and α_{BC} are the coefficients of thermal expansion of the substrate and the bond coating, respectively. γ_{BC} is the ratio of the bond coating and the substrate stiffness, γ_{TC} is the ratio of top coating and substrate stiffness, and ΔT is the difference between operating and room temperatures.

It should be noted that while the influence of elastic strain, thermal expansion deformation, and bending deformation are considered in Eqs. (2), (3), this implies that the structure is fully dense (i.e. no porosity). However, upon closer examination, it is apparent that the structural influence of a porous network in the TBC system is not included. Owing to the relatively low thickness of the top coatings (~200 μm) relative to the substrate, the thermal stress can be defined using a plane strain model, and a single micro-pore can be used to simplify the analysis. As illustrated in Fig. 1, the circle and the square represent the micro-pore and the matrix of the top coating, respectively. The single micro-pore is assumed to be far away from the boundary and the other micro-pores (≫2.5 times the radius of micro-pores) of the coating. The stress f_1 is uniformly distributed around the circle because of the compression and expansion of internal gas that is contained within the pore. In addition, the surrounding stress (f_2 and f_3) show that TBC systems are anisotropic, this is attributed to the thermal spray technique that is used to deposit the layers. In part I, the stresses at the interface can be described using the following equations [16]:

(4)

$$\sigma_\rho = -\frac{r^2}{\rho^2}f_1$$

(5)

$$\sigma_\varphi = \frac{r^2}{\rho^2}f_1$$

where σ_ρ is the radial stress, σ_φ is the circumferential stress, r is the radius of the micro-pores, and ρ is the polar radius. According to the Kirsch equations derived from the theory of elasticity, the following formulas are introduced to describe the summary stresses in parts II and III [17].

(6)

$$\sigma_\rho = -\frac{f_2 + f_3}{2}\left(1 - \frac{r^2}{\rho^2}\right) + \frac{f_3 - f_2}{2}\left(1 - \frac{r^2}{\rho^2}\right)\left(3\frac{r^2}{\rho^2} - 1\right)\cos 2\varphi$$

(7)

$$\sigma_\varphi = -\frac{f_2 + f_3}{2}\left(1 + \frac{r^2}{\rho^2}\right) + \frac{f_3 - f_2}{2}\left(3\frac{r^4}{\rho^4} + 1\right)\cos 2\varphi$$

where φ is the polar angle.

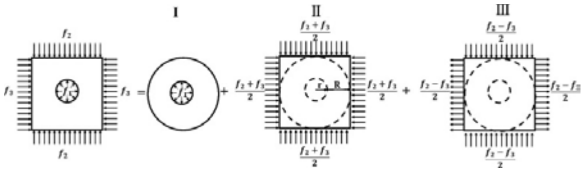

Fig. 1. Schematic representation of a single pore model in closed-form analysis.

Based on the principle of superposition, Eqs. (4), (5), (6), (7) can be combined and the following equations obtained for the radial and circumferential stress:

(8)

$$\sigma_\rho = -\frac{r^2}{\rho^2} f_1 - \frac{f_2 + f_3}{2}\left(1 - \frac{r^2}{\rho^2}\right) + \frac{f_3 - f_2}{2}\left(1 - \frac{r^2}{\rho^2}\right)\left(3\frac{r^2}{\rho^2} - 1\right)\cos 2\varphi$$

(9)

$$\sigma_\varphi = \frac{r^2}{\rho^2} f_1 - \frac{f_2 + f_3}{2}\left(1 + \frac{r^2}{\rho^2}\right) + \frac{f_3 - f_2}{2}\left(3\frac{r^4}{\rho^4} + 1\right)\cos 2\varphi$$

To further analyze the effect of micro-pores, four different polar radii were selected. The resulting stresses obtained using Eqs. (8), (9) results are shown in Table 3; they indicate that the single micro-pore model has the features of centrality and locality. The hoop stress near the hole side significantly decreased with an increase in the polar radius. The value of the maximum hoop stress was calculated to be up to three times higher than that of its surrounding area, and also satisfies Saint-Venant's principle.

Table 3. The equations of hoop stress around the micro-pore.

ρ	**r**	**2r**	**3r**	**4r**
σ90°	$-3f_3 + f_1 + f_2$	$-f_3 - \frac{7f_3 - 8f_1 + f_2}{32}$	$-f_3 - \frac{4f_3 - 6f_1 + 2f_2}{54}$	$-f_3 - \frac{19f_3 - 32f_1 + 13f_2}{512}$

4. FE simulation model

The effect of micro-pores on the mechanical field in the TBC was analyzed using the commercially available FE software ANSYS 15.0. As details regarding the ANSYS formulation are well known, only a summary of the model is provided here. The FE model consisted of three layers which included: a 200 µm-thick top coat, 100 µm-thick bond coat, and a 3000 µm-thick substrate (K406). Randomly distributed micro-pores were placed in top coat. The 2D plane strain element was used in the simulation. The geometry structure and relevant boundary conditions were established for the tested samples, as shown in Fig. 2. Here, the x and y directions correspond to the radial and axial directions of the sample, respectively. The abovementioned model, whose parameters were derived from practical experiments, ensures the effectiveness and correctness of the proposed methods. To describe the porous structure of the TC more accurately, a stochastic based restructuring technique, called the random generate method, was used to generate a porous structure. In the simulation, the radius of the circles was randomly set (limited to the range 3–5 µm), with a random distribution of center points. To ensure precise calculation and computing power, the width (2000 µm) was set to ten times the thickness of the TC. The morphology of cracks and micro-pores in the TC is a crucial parameter affecting the thermal and mechanical properties of coatings. Finally, the actual micromechanical model is established which is based on the cross-section image of the YSZ coatings.

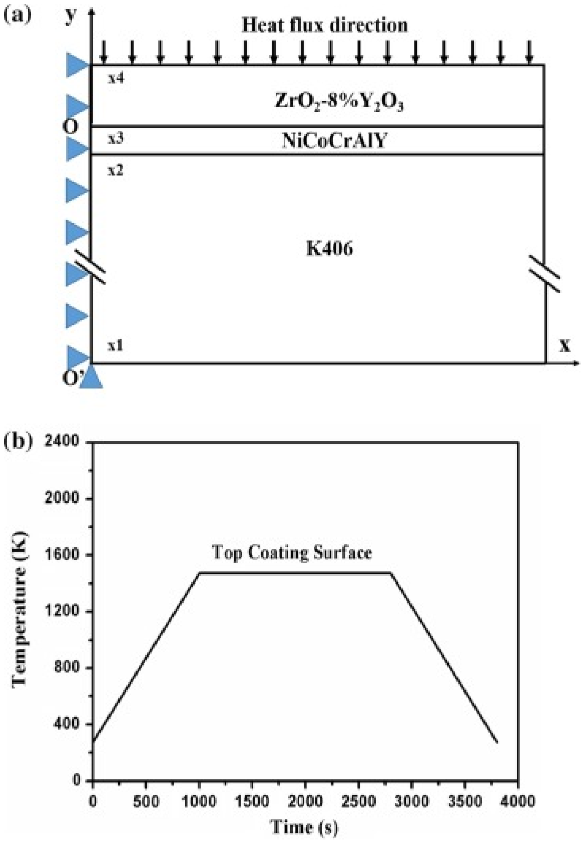

Fig. 2. Schematic representation of (a) the TBC model, and (b) thermal loading history used in the FE analysis.

The heat transfer interface acts as a thermal load for the structural simulation, causing thermal expansion or contraction. During the simulations, heat flow at 1473 K was introduced on the top surface for 30 min (Fig. 2c). The details of the physical properties used to represent each material are given in Tables 4 [7], [9], [18], [19], [20], [21], [22]. Because plastic deformation represents a possible stress-relaxation mechanism in bond coating and substrate, the elastic-plastic properties were used in the calculation with bilinear hardening behavior being assumed. In addition, all layers are assumed to be combined with creep-plastic materials. The 2D FE model of micro-pores was prepared, and the mesh around the TC/micro-pore interface was confirmed to be sufficiently fine by independent test (Fig. 3). The independent test of porous thermal barrier coating selects four different parameters, which are the number of element division, are shown in Fig. 2b. When the parameters are changed, the total mesh, the maximum radial stress, are shown in Table 5. It can be seen that when the number of mesh is mesh3, the computational domain of mesh3 is the smallest. And the maximum radial stress of the target surface compared to mesh 4 does not change the substance. Therefore, selecting the mesh3 as the minimum calculation domain will not affect the results due to the number of mesh.

Table 4. Thermophysical properties of the substrate, bond coating and top coating materials used in the study [7], [9], [18], [19], [20], [21], [22].

Materials	**Temperature (K)**	**Thermal conductivity [W/(m·K)]**	**Young modulus (GPa)**	**Linear coefficient of thermal expansion (10^{-6}·K^{-1})**	**Poisson's ratio**	**Yield strength (MPa)**	**Tangent modulus (GPa)**	**Creep coefficient**	**Creep index**
K406C	273	11.30	189	15.76	0.26	560	1.7	2.2×10^{-14}	3
	473	12.56	182		0.25				
	673	15.49	173		0.25				
	873	18.84	163		0.27				
	1073	22.29	150		0.29				
	1273	22.61	149		0.32				
	1473	22.61	149		0.32				
NiCoCrAlY	273	4.3	186	14.3	0.3	270	0.69	1.4×10^{-14}	3
	673	6.4							
	1073	10.2							
	1473	11.1							
ZrO_2-8 wt.%Y_2O_3	273	2.42	45	10.2	0.1			1.8×10^{-11}	0.48
	473	2.48							
	673	2.43							
	773	2.41							
	1273	1.6							
	1473	1.6							

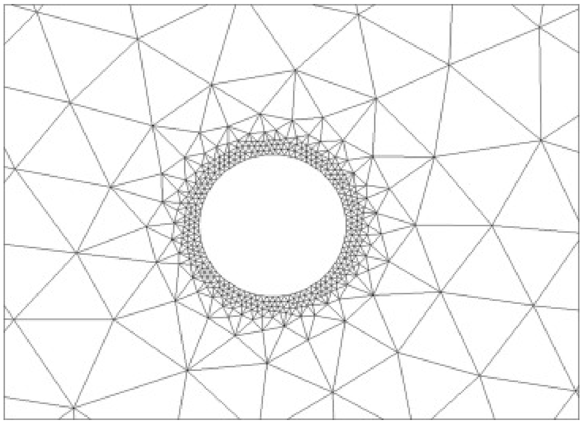

Fig. 3. Schematic showing FE mesh refinement used to model individual micro-pores in the ceramic layer of the TBC.

Table 5. Parameters associated with different meshes used for independent test.

Mesh	**x_1**	**x_2**	**x_3**	**x_4**	**Total mesh**	**Maximum radial stress (GPa)**
1	100	200	400	400	305 227	1.57
2	100	200	400	500	367 339	1.72
3	100	250	500	500	416 286	1.81
4	150	250	500	550	453 588	1.86

5. Results and discussion

5.1. Microstructure

The cross-sectional morphology and the porosity of the as-deposited ZrO_2-8 wt.%Y_2O_3 top layer is shown in Fig. 4. It can be seen that the coating microstructure is not uniform and that numerous inter-lamellar micro-pores are also visible because the adjacent splats do not overlap fully. In addition, the gas dissolved in the plasma jet will penetrate into the molten or semi-molten state of the droplet. Further, the small bubbles are not afforded a timely escape owing to the decrease in the solubility when single splats are sputtered onto the substrate, and pores can also be produced. However, this unique feature of the thermal spray deposition process also contributes to a further decrease in thermal conductivity due to the presence of the pores. The porosity values (approximately 4.87%) and the pore-size distribution of the TC were determined using the digital image capture and analysis method. The calculated result (Fig. 4b) which showed that the majority of the voids were randomly oriented isolated micro-pores with a narrow size distribution. An analysis of the micro-pore size of the TC showed that 83.4% of the micro-pores had a radius between 3 and 5 µm, while the remaining 6.73% had a radius below 3 µm, including nano-sized micro-pores. The remainder of the micro-pores had a radius exceeding 5 µm. To analyze the effect of porosity, porosity values of 1, 3, and 5% were tested (Fig. 5). The porosity values of 3 and 1% were chosen to represent the TC that exhibited densification due to the healing of the micro-pores and sintering phenomena that occurred during high-temperature processing. In order to study the influence of micro-defects on residual stress, the geometry of the cross-section profile (Fig. 6) was carefully reconstructed according to the real microstructural features such as micro-pores, splats, and cracks taken from SEM micrographs of coating cross-section.

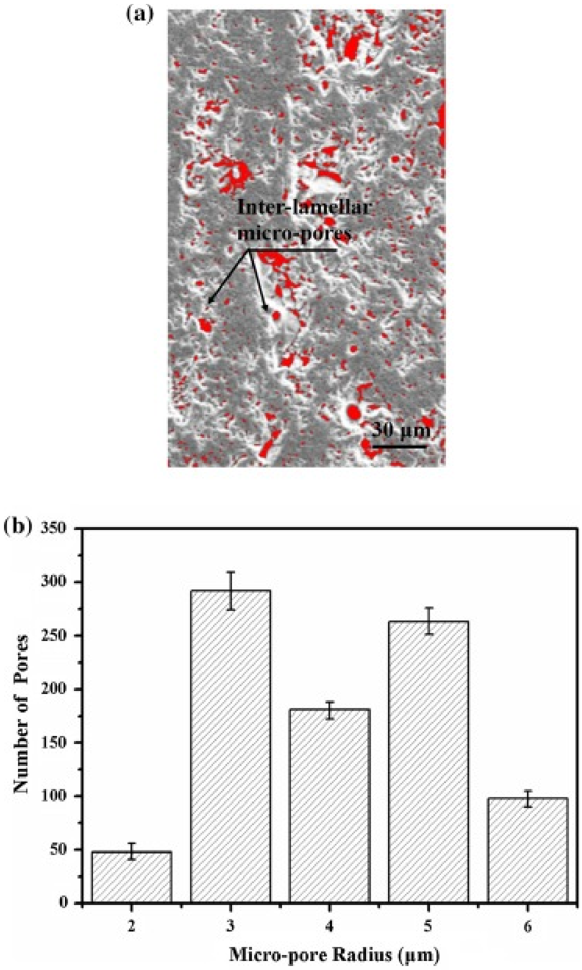

Fig. 4. SEM micrograph showing (a) the cross-sectional morphology, and (b) pore-size distribution of the ZrO_2-8 wt% Y_2O_3 ceramic top coating.

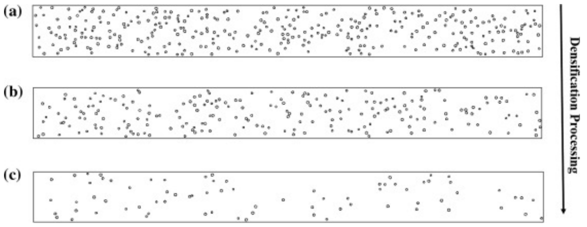

Fig. 5. Schematic representation of void geometry and distribution at (a) 5%, (b) 3%, and (c) 1% porosity levels.

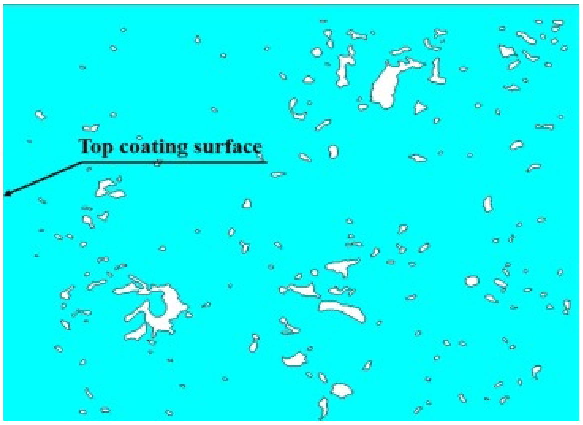

Fig. 6. Modeling representation of ceramic top coating based on the cross-sectional image.

5.2. Simulation results

In this section, the thermal stress distribution is discussed in detail by comparing the FE simulation results and the closed-form analysis. The sign convention used here is that compressive stress is negative and tensile stresses are positive values. Fig. 7 shows the radial stress field of a solid TBC (i.e. 0% porosity) at 1473 K. It is evident that the top coating was under tensile stress; however, the bond coating and the substrate exhibited compressive stress under real service conditions. The thermal expansion of the coating surface was unrestricted, however, the lower layers slowed the effective free expansion. The radial stress-position curve at the coating surface is shown in Fig. 7b. All of them are free elements at the right edge; the deformation can transfer to the free edge and release the energy in time. As a result, the value of radial stress showed a retardation trend near the right edge. The accuracy of the FE models (without defects) was also verified by comparing the computational result and the closed-form calculation of thermal stress. The simulation result of stress obtained at the TC surface has an average value of 314 MPa which shows good agreement with the theoretical value of 324 MPa obtained from Eq. (3). According to the above results, the boundary condition and the parameters of the established models are verified to be correct. Fig. 8 shows the stress distribution after the substrate and the sprayed materials were cooled to the 293 K. There is overall compressive stress in the top coating, and the average radial stress at the surface is −210.37 MPa (Fig. 8b). However, the maximum tensile stress (137 MPa) is generated at the top/bond coatings interface because of the mismatch in the coefficient of thermal expansion. The irreversible nature of plastic deformation within the TBC led to an inverted stress distribution. This is the principal reason for the failure of TBC coatings, resulting in the spallation of the top coating when turbine blades are operated under the service condition.

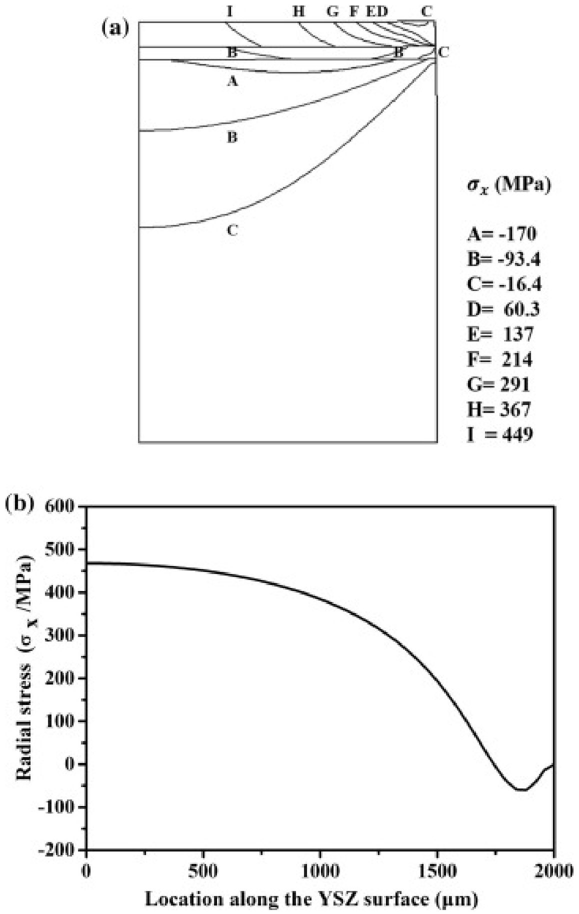

Fig. 7. Calculated radial stress distribution obtained from solid TBC of (a) the whole part and (b) the coating surface at 1473 K.

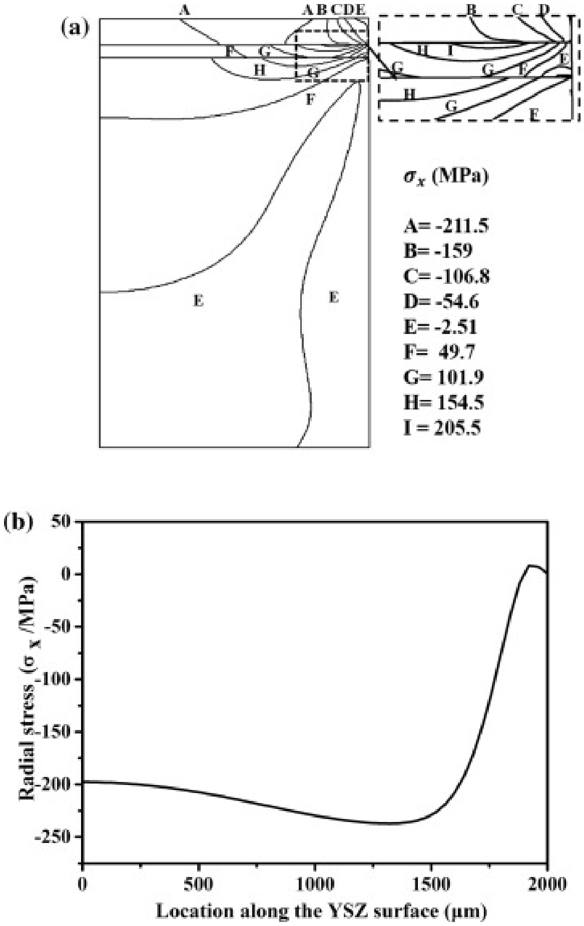

Fig. 8. Calculated radial stress distribution obtained from solid TBC of (a) the whole part and (b) the coating surface at 293 K.

The FE results indicate that the tensile stress existed within the porous TC when heated to 1473 K (Fig. 9). During densification processing, the average value of stress increased from 265 to 308 MPa within the whole TC. In the axial direction, the maximum stress (1487 MPa) near the micro-hole edge is approximately three times higher than that of the surrounding area (Fig. 10), in accordance with the results in Table 1. In the sustained high temperature, the tensile stress would exceed the yield points of the materials and result in permanently deform. The isolated micro-hole was squeezed and released the deformation energy to the TC surface or TC/BC interface along the axial direction, which played an important role in the mechanisms of crack initiation.

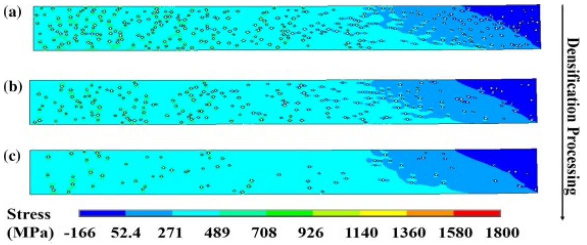

Fig. 9. Simulated radial stress contours obtained at 1473 K from the FE model at of (a) 5%, (b) 3%, and (c) 1% porosity levels.

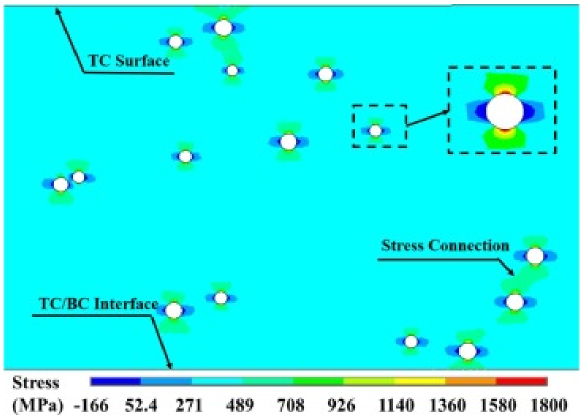

Fig. 10. Simulated results showing radial stress field at 1473 K for a porosity of 1%

After cooling to 273 K, the porous TC will switch from a tensile stress state to a compressive state owing to the CTE. The radial stress of TC is lower than that of the solid one (porosity 0%) also because of the deformation of micro-pores as a stress–relaxation mechanism in the as-sprayed coatings (Fig. 11). When the level of porosity is above 3%, the stress-affected areas are prone to connect in the radial direction. The average value of the compressive stress increased from −127.8 to −175.4 MPa, while the porosity sintered from 5 to 1%. Tanaka et al. [23] also calculated the value of residual stress (−270 to −120 MPa) by micro-Raman spectroscopy. It was proved that the simulation results are reliable and accurate. However, the micro-hole edge maintains the tensile stress state in the radial direction, which suggests that radial cracks still propagate during the cooling process (Fig. 12). As a result, spallation will occur within TC. When the level of porosity is 1%, a single micro-pore formed in the stress-affected area, which is almost isolated owing to the distance between neighboring micro-pores.

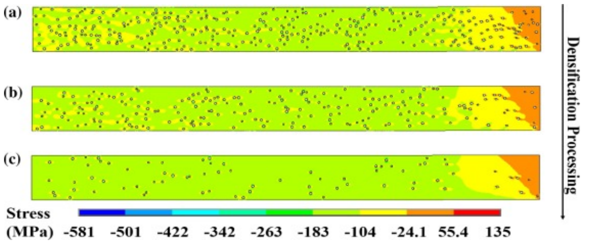

Fig. 11. Simulated radial stress contours obtained from the FE model at porosity levels of (a) 5%, (b) 3%, and (c) 1% at 293 K.

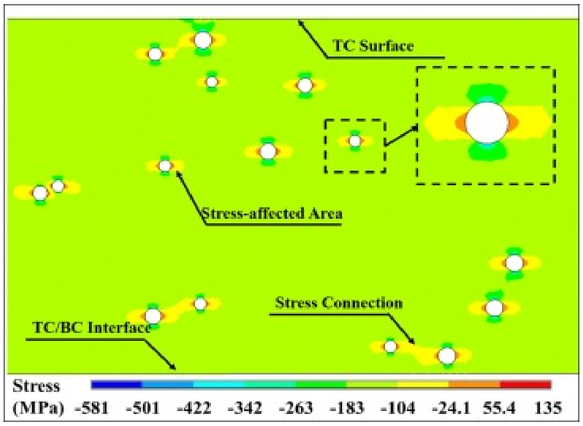

Fig. 12. Simulated results showing radial stress for the porosity of 1% at 293 K.

The creep and plastic deformations can simultaneously develop at suitable stress levels. For creep behavior of all layers, the following creep model is used [24]:

(10)

$$\varepsilon = C\sigma^{n}$$

where ε is the uniaxial equivalent creep strain rate, σ is Von Mises equivalent stress. C and n are the creep coefficient and creep index, respectively. The creep and plastic deformations, as well as the thermal mismatch, dominate the stress development. The time-dependent evolution with the four different porosities are evaluated (Fig. 13), to show how the creep strain evolve. With the increase of porosity, the creep strain is decreased. The direct reason is that the micro-pores affect the stress distribution characteristic and the stress magnitude. The thermal barrier coating with high levels of porosity can resist high temperatures and reduce creep deformation after working a long time.

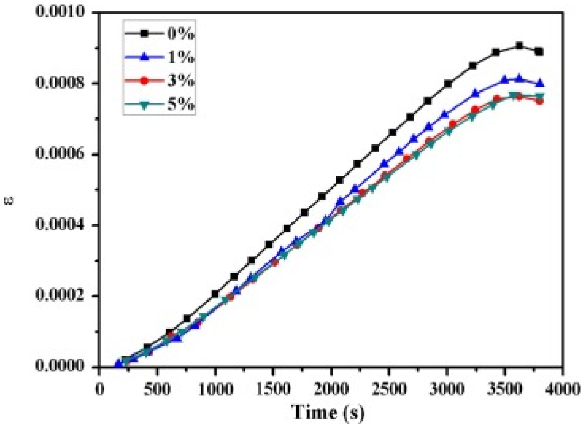

Fig. 13. Evolution of the maximum equivalent creep strain of top coating.

According to the simulation results of image-based modeling (Fig. 14), it can be seen that the maximum tensile stress (1872 MPa) appears at the crack tip at 1473 K. During the service condition, the micro-pores in the top coating can affect the residual stress distribution in the local area around the cracks. In addition, the inner of the porous TC also has some connections between cracks and micro-pores that affect the stress distribution and magnitude. As for the cracks, the radial crack, axial crack, and crack length will also affect the failure behavior of the TBCs. Some branched cracks will be formed at the interface between two contiguous upward and underlying splats [25]. The micro-cracks will propagate, link at the axial direction and then reach the TC/BC interface eventually, then the failure of the coating will occur.

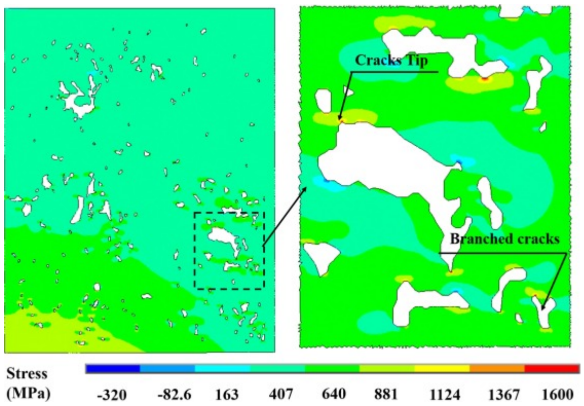

Fig. 14. Simulated results showing radial stress for image-based modeling in the top coating.

The different levels of porosity and the service environment may cause two different types of micro-cracks in the ceramic top layer which include: (1) radial cracks within ceramic coatings from the interactions of neighboring micro-pores; (2) axial cracks that are easily initiated near the surface because of tensile stress propagating radially during the heating stage. A radial crack will form when the porosity reaches above 3% owing to the overlap of the affected stress area. After the cooling stage, the radial cracks will continue propagating. As a result, coating spallation may occur, especially along the top/bond coating interface (Fig. 15a). This region can easily store the elastic strain energy, and the energy release rate for a crack is also increased because the different materials exist at the interface. In addition, the micro-pores that exist near the interface enforce coating spallation because the connected area of tensile stress promotes crack propagation, and the surrounding high-stress state further increases the stress intensity of the radial crack. If the top coating has low porosity, below 3%, or suffered crashed particles (CMAS) at high temperature, micro-cracks may propagate through the micro-pores that are near the surface, finally reaching the top/bond coat interface (Fig. 15b). This is attributed to the higher in-plane tensile stress; single micro-pores have an important influence in the axial direction. The affected area is hardly connected in the radial direction when the porosity is below 3%. On the one hand, radial cracks can relax the thermal stresses and improve the strain tolerance within the top coating and cracks may be closed during the cooling stage. On the other hand, the durability of the TBC is limited because of their susceptibility to corrosion caused by vanadium salts or oxidation in practice. Overall, the increased porosity will decrease the whole stress level and may eventually delay the propagation rate of the main cracks.

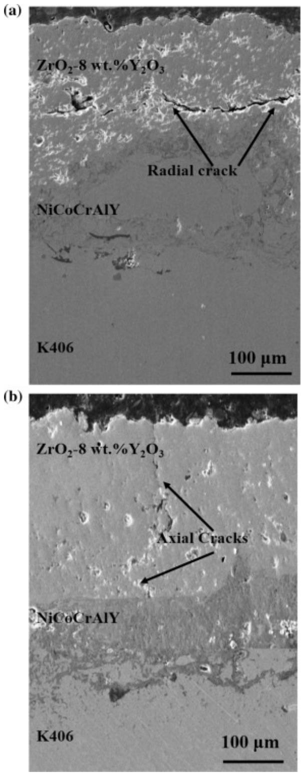

Fig. 15. SEM micrograph showing cross-sectional morphology of the TBC: (a) axial cracks and (b) radial cracks.

Fig. 16 shows the stress distribution of the TC surface at 1473 K. All the radial stress-position curves show a moderating trend because the energy is released completely at the right edge. The “jump” phenomenon of stress appears in the micro-pores-affected area because the plastic-elastic behavior resulted in a very high tensile stress in transient analysis. When the TC surface suffers particle collisions such as calcia-magnesia-alumino-silicate (CMAS) during service life, the cracks may penetrate to the TC/BC interface quickly. In particular, the sintered TC maintains the highest tensile state (porosity < 3%), which results in coating failure. After cooling to the room temperature, the radial stress-position curves suggest that the surface is in a compressional environment. The “drop” phenomenon of stress appears at regions around the micro-pores because of contraction distortion (Fig. 17). The bottom value is approximately two times higher than the surrounding area depending on the distance between the surface and the micro-pores.

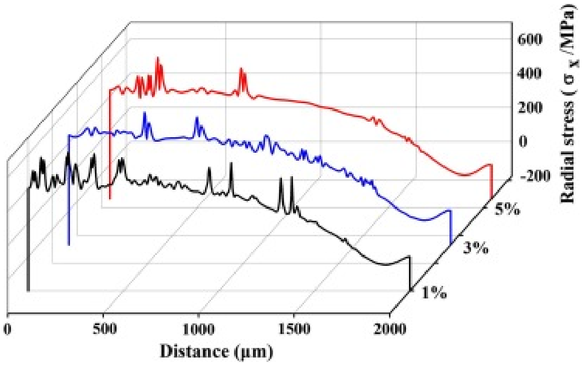

Fig. 16. Radial stress-position curve of the top coating surface at 1473 K.

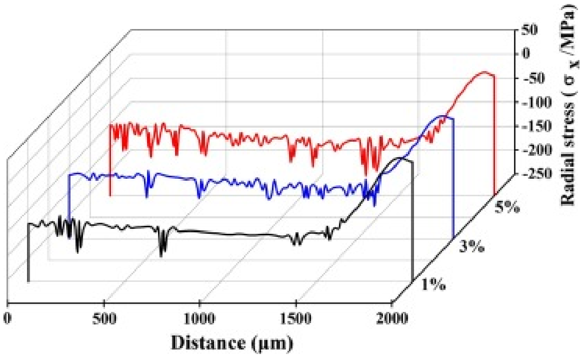

Fig. 17. Radial stress-position curve of the top coating surface at 293 K.

The FE analysis of YSZ coatings at different porosity levels shows that the stress concentration phenomenon of the micro-pores will increase the stress value near-surface region. When the coating surface subjected to particle impact, the axial cracks expand along the stress concentration area. The results of a single micro-pore analysis show that the range of affected areas is three times than of its own radius. Therefore, a sealed layer with a thickness of 20 μm was added to investigate the effect on the surface stress state of the YSZ coating. Fig. 18 shows the radial stress curve on the outer contour of the sealed YSZ at 1473 K. The stress curve still maintains a downward trend on the right side suggested the overall surface stress state of the sealed YSZ coating does not change greatly. However, the 5%, 3%, and 1% radial curves become smoother, indicating that the addition of a 20 μm sealing layer effectively eliminates the stress effects of the micro-pores on the YSZ coating surface. When the temperature drops to 293 K, the radial stress curve on the outer contour of the sealed YSZ is shown in Fig. 19. The smoothing effect of the sealing layer also appears on the stress curve. In our previous study [26], the Al-Y/YSZ layered design ensured the maintenance of high porosity within the YSZ coating, allowing the coating to retain its superior thermal isolation performance and improving the oxidation resistance.

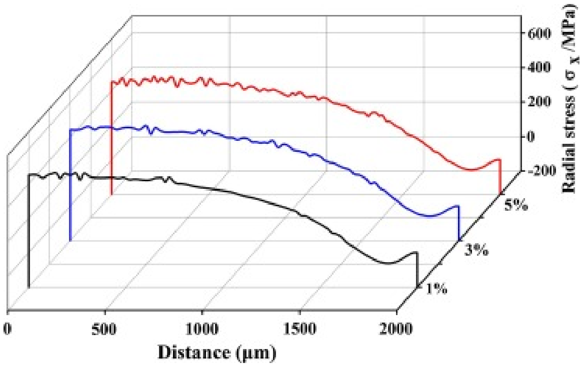

Fig. 18. Radial stress-position curve of the sealed coat surface at 1473 K.

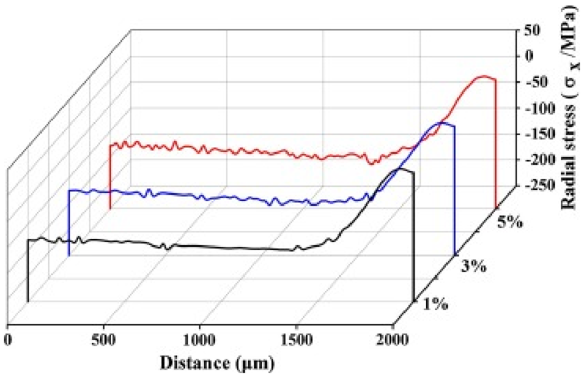

Fig. 19. Radial stress-position curve of the sealed coat surface at 293 K.

5.3. Nano-indentation results

The nanoindentation technique was utilized to measure the thermal stress state of the top coating, and it provided a qualitative assessment of the stress distribution obtained using the FE method. The indentation load-displacement curve is shown in Fig. 20. With an increase in the load, the plastic deformation was increased in steps, which is a non-linear loading process. However, the unloading process is irreversible because of the recovery period of materials. The load-displacement curve of the stressed sample is shown on the right side of that of the unstressed TBC, which suggests that compressive stress remained within the coating. During the indentation process, the pressure stress from the indenter is perpendicular to the surface of the specimen. If the specimen has inner compressive stress, the direction of the compressive stress is opposite to that of the shear stress caused by the indenter. As a result, the compressive stress will obstruct the penetration of the indenter and the penetration depth will decrease. A theoretical model using a geometrically similar sharp indenter has been proposed by Suresh and Giannakopoulos for the determination of equi-biaxial stress [27]. When the load is fixed, the compressive stress can be calculated by the following equation:

(11)

$$\sigma = \frac{H_d}{sin\alpha}\left(\frac{h^2}{h_0^2} - 1\right)$$

where H_d is the dynamic hardness of the TBC under stress-free state (around 5.41 GPa), α is the pressure angle (32.5°), and h and h_0 represent the indenter displacement of the unstressed and the compressively stressed samples when the load reaches 100 mN, respectively. The indenter displacement of the unstressed and the compressively stressed samples are 2.99 and 2.96 μm, respectively. Based on the above data, the value of inner stress is calculated to be −230.2 MPa at 3 μm below the surface. This lowers the FE result (175.4 MPa) because the surface of the top coating is totally sintered after heat processing. Furthermore, the real contact area between the indenter and the coating surface is smaller than the values obtained during the experiment.

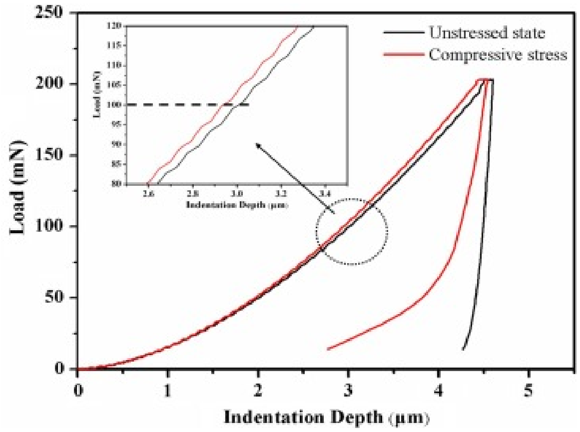

Fig. 20. The indentation load-displacement curve of the top coating.

6. Conclusion

In this study, an FE model of a TBC containing a porous ceramic top coating was developed based on a quantitative image analysis of plasma-sprayed samples and was used to investigate the effect of porosity on stress distribution and magnitude. Based on the results that were obtained, the following conclusions can be made:

(1) The thermal spray process resulted in the formation of well-aligned pores with a narrow pore-size distribution (3–5 μm radius) in ceramic coating.
(2) In the porous system, a single pore affected the structure field over a limited area (below 3 times the pore radius) which is in accordance with Saint-Venant’s principle.
(3) According to the FE results and the nanoindentation tests, the whole top coating shows compressive stress which remained within the layers and was manifested as residual stresses during cooling at room temperature. Furthermore, the compressive stress level tends to decrease with an increase in the number of micro-pores or porosity.
(4) Based on the nucleation of micro-cracks, axial cracks that penetrate to the top/bond coating interface are generated when the porosity is below 3%. However, with an increase in the percentage of porosity, the type of cracks changes to radial cracks at the top/bond coating interface. The results also suggest that the porosity and service environment may affect the crack growth orientation.

Author contributions

Shiyu Cui took the lead in writing the manuscript. Shiyu Cui and Wenping Liang conceived of the presented idea. Shiyu Cui and Qiang Miao developed the theory and performed the computations. Luis Saucedo Mora and Joseph P. Domblesky. helped carry out the FE simulations. Shiyu Cui and Hao Lin verified the analytical methods. Shiyu Cui and Lijia Yu carried out the experiment. Shiyu Cui wrote the manuscript with support from Luis Saucedo Mora and Joseph P. Domblesky. All authors discussed the results and contributed to the final manuscript.

Declaration of Competing Interest

The authors declared that there is no conflict of interest.

Acknowledgment

The authors gratefully acknowledge financial support from the China Scholarship Council. This study was supported by a project funded by the National Natural Science Foundation of China (No. 51474131), the program of China Scholarships Council (No. 201706830067), the Priority Academic Program Development of Jiangsu Higher Education Institutions (PADA), and Graduate Research and Innovation Projects in Jiangsu Province (Grant No. KYLX16 0349).

References

[1] B. Lv, H. Xie, R. Xu, X. Fan, W. Zhang, T.J. Wang. **Effects of sintering and mixed oxide growth on the interface cracking of air-plasma-sprayed thermal barrier coating system at high temperature.** *Appl. Surf. Sci.,* 360 (2016), pp. 461-469

[2] N. Zotov, M. Bartsch, L. Chernova, D.A. Schmidt, M. Havenith, G. Eggeler. **Effects of annealing on the microstructure and the mechanical properties of EB-PVD thermal barrier coatings.** *Surf. Coat. Technol.,* 205 (2010), pp. 452-464

[3] M. Gupta, N. Curry, P. Nylén, N. Markocsan, R. Vaßen. **Design of next generation thermal barrier coatings—Experiments and modelling.** *Surf. Coat. Technol*., 220 (2013), pp. 20-26

[4] L. Wang, D.C. Li, J.S. Yang, F. Shao, X.H. Zhong, H.Y. Zhao, K. Yang, S.Y. Tao, Y. Wang. **Modeling of thermal properties and failure of thermal barrier coatings with the use of finite element methods: a review.** *J. Eur. Ceram. Soc*., 36 (2016), pp. 1313-1331

[5] C. Li, X. Zhang, Y. Chen, J. Carr, S. Jacques, J. Behnsen, M. di Michiel, P. Xiao, R. Cernik. **Understanding the residual stress distribution through the thickness of atmosphere plasma sprayed (APS) thermal barrier coatings (TBCs) by high energy synchrotron XRD; digital image correlation (DIC) and image based modelling.** *Acta Mater*., 132 (2017), pp. 1-12

[6] Y. Chai, C. Lin, Y. Li. **Effects of creep-plastic behavior on stress development in TBCs during cooling.** *Ceram. Int.,* 43 (2017), pp. 11627-11634

[7] Y.C. Zhou, T. Hashida. **Coupled effects of temperature gradient and oxidation on thermal stress in thermal barrier coating system.** *Int. J. Solids Struct*., 38 (2001), pp. 4235-4264

[8] J. Zhang, X. Guo, Y.-G. Jung, L. Li, J. Knapp. **Lanthanum zirconate based thermal barrier coatings: a review.** *Surf. Coat. Technol*., 323 (2017), pp. 18-29

[9] S. Widjaja, A.M. Limarga, T.H. Yip. **Modeling of residual stresses in a plasma-sprayed zirconia/alumina functionally graded-thermal barrier coating.** *Thin Solid Films*, 434 (2003), pp. 216-227

[10] J. Zhu, H. Xie, Z. Hu, P. Chen, Q. Zhang. **Cross-sectional residual stresses in thermal spray coatings measured by Moiré interferometry and nanoindentation technique.** *J. Therm. Spray Technol*., 21 (2012), pp. 810-817

[11] L. Wang, F. Shao, X.H. Zhong, J.X. Ni, K. Yang, S.Y. Tao, Y. Wang. **Tailoring of self-healing thermal barrier coatings via finite element method.** *Appl. Surf. Sci.,* 431 (2018), pp. 60-74

[12] Y. Song, X. Zhuan, T.J. Wang, X. Chen. **Evolution of thermal stress in a coating/substrate system during the cooling process of fabrication.** *Mech. Mater.,* 74 (2014), pp. 26-40

[13] M. Bäker, P. Seiler. **A guide to finite element simulations of thermal barrier coatings.** *J. Therm. Spray Technol*. (2017), pp. 1-15

[14] S. Kuroda, T.W. Clyne. **The quenching stress in thermally sprayed coatings.** *Thin Solid Films*, 200 (1991), pp. 49-66

[15] X. Shu, R. Wang. **Thermal residual solutions of beams, plates and shells due to laminated object manufacturing with gradient cooling.** *Compos. Struct*., 174 (2017), pp. 366-374

[16] Z. Xu. ***Applied Elasticity.*** Wiley (1992)

[17] G. Kirsch. ***Die Theorie der Elastizität und die Bedürfnisse der Festigkeitslehre.*** Springer (1898)

[18] L. Wang, Y. Wang, X.G. Sun, J.Q. He, Z.Y. Pan, Y. Zhou, P.L. Wu. **Influence of pores on the thermal insulation behavior of thermal barrier coatings prepared by atmospheric plasma spray.** *Mater. Design*, 32 (2011), pp. 36-47

[19] L. Wang, Y. Wang, W.Q. Zhang, X.G. Sun, J.Q. He, Z.Y. Pan, C.H. Wang. **Finite element simulation of stress distribution and development in 8YSZ and double-ceramic-layer La2Zr2O7/8YSZ thermal barrier coatings during thermal shock.** *Appl. Surf. Sci*., 258 (2012), pp. 3540-3551

[20] C. Nordhorn, R. Mücke, K.A. Unocic, M.J. Lance, B.A. Pint, R. Vaßen. **Effects of thermal cycling parameters on residual stresses in alumina scales of CoNiCrAlY and NiCoCrAlY bond coats.** *Surf. Coat. Technol*., 258 (2014), pp. 608-614

[21] H.W. Ng, Z. Gan. **A finite element analysis technique for predicting as-sprayed residual stresses generated by the plasma spray coating process.** *Finite Elem. Anal. Des*., 41 (2005), pp. 1235-1254

[22] J. Rösler, M. Bäker, K. Aufzug. **A parametric study of the stress state of thermal barrier coatings: Part I: creep relaxation.** *Acta Mater*., 52 (2004), pp. 4809-4817

[23] M. Tanaka, R. Kitazawa, T. Tomimatsu, Y.F. Liu, Y. Kagawa. **Residual stress measurement of an EB-PVD Y2O3-ZrO2 thermal barrier coating by micro-Raman spectroscopy.** *Surf. Coat. Technol*., 204 (2009), pp. 657-660

[24] Q.M. Yu, L. Cen. **Residual stress distribution along interfaces in thermal barrier coating system under thermal cycles.** *Ceram. Int*., 43 (2017), pp. 3089-3100

[25] L. Wang, X.H. Zhong, F. Shao, J.X. Ni, J.S. Yang, S.Y. Tao, Y. Wang. **What is the suitable segmentation crack density for atmospheric plasma sprayed thick thermal barrier coatings with the improved thermal shock resistance?** *Appl. Surf. Sci*., 431 (2018), pp. 101-111

[26] S. Cui, L. Saucedo-Mora, W. Liang, Q. Miao, Y. Xu. **Beneficial effects of magnetron-sputtered Al–Y seal layers on porous thermal barrier coatings.** *J. Alloys Compd*., 804 (2019), pp. 147-154

[27] S. Suresh, A.E. Giannakopoulos. **A new method for estimating residual stresses by instrumented sharp indentation.** *Acta Mater*., 46 (1998), pp. 5755-5767